Original Research Article

Rapid distortion correction enables accurate magnetic resonance imaging-guided real-time adaptive radiotherapy

Paul Z. Y Liu [a,b], Shanshan Shan [a,b], David Waddington [a,b], Brendan Whelan [a,b], Bin Dong [b], Gary Liney [b,c,d], Paul Keall [a,b,*]

[a] Image X Institute, University of Sydney Central Clinical School, Sydney, NSW, Australia
[b] Department of Medical Physics, Ingham Institute for Applied Medical Research, Liverpool, NSW, Australia
[c] School of Medicine, University of New South Wales, Sydney, NSW, Australia
[d] Centre for Medical Radiation Physics, University of Wollongong, Wollongong, NSW, Australia

A R T I C L E   I N F O

A B S T R A C T

Background and purpose: Magnetic resonance imaging (MRI)-Linac systems combine simultaneous MRI with radiation delivery, allowing treatments to be guided by anatomically detailed, real-time images. However, MRI can be degraded by geometric distortions that cause uncertainty between imaged and actual anatomy. In this work, we develop and integrate a real-time distortion correction method that enables accurate real-time adaptive radiotherapy.

Materials and methods: The method was based on the pre-treatment calculation of distortion and the rapid correction of intrafraction images. A motion phantom was set up in an MRI-Linac at isocentre (P_0), the edge (P_1) and just outside (P_2) the imaging volume. The target was irradiated and tracked during real-time adaptive radiotherapy with and without the distortion correction. The geometric tracking error and latency were derived from the measurements of the beam and target positions in the EPID images.

Results: Without distortion correction, the mean geometric tracking error was 1.3 mm at P_1 and 3.1 mm at P_2. When distortion correction was applied, the error was reduced to 1.0 mm at P_1 and 1.1 mm at P_2. The corrected error was similar to an error of 0.9 mm at P_0 where the target was unaffected by distortion indicating that this method has accurately accounted for distortion during tracking. The latency was 319 ± 12 ms without distortion correction and 335 ± 34 ms with distortion correction.

Conclusions: We have demonstrated a real-time distortion correction method that maintains accurate radiation delivery to the target, even at treatment locations with large distortion.

1. Introduction

The introduction of MRI-Linacs into the modern radiation therapy has taken image-guidance to a new level of precision. MRI provides the ability to distinguish between malignant and healthy tissues and MRI-Linacs can simultaneously acquire MRIs during radiation delivery [1]. MRI-Linacs enable real-time beam adaptation techniques such as beam gating [2] and multi-leaf collimator (MLC) tracking [3,4] that account for anatomic motion during radiation delivery. These techniques can ensure the accurate delivery of radiation [5], but successful integration requires precise real-time localisation of the target, particularly when combined with highly conformal and dynamic treatment modalities such as IMRT or VMAT [6].

While MRI-guided radiotherapy has many advantages, one drawback that can affect the accuracy of this localisation is geometric distortion [7]. Geometric distortion can be caused by a number of system-related factors, the most prevalent of which is gradient non-linearity (GNL). MR images are reconstructed on the premise that the gradient magnetic fields responsible for spatial encoding of the MR signal vary linearly across the imaging field. In practice, a perfectly linear gradient field is not achievable due to manufacturing and engineering limitations. Discrepancies between the real and expected gradient fields will cause mis-

mapping of pixels in the reconstructed image.

Existing methods to account for GNL distortion are well documented in the literature [8,9]. One common method to characterise the GNL field within the imaging volume is with polynomial functions such as spherical harmonic expansions or spline models. Once an accurate characterisation of the GNL field has been obtained, geometric distortions can subsequently be corrected by using coordinate mapping and intensity scaling. This image domain distortion correction method provides a fast distortion correction and has been widely adopted on most commercial MR scanners through vendor supplied corrections. After the vendor correction is applied, distortion is generally well managed at and near the isocentre, but increases with off-axis distance [10–13].

Accounting for geometric distortion, including the residual distortion that exists after vendor correction, is essential for MRI-Linacs. First and foremost, these MRIs are used to guide radiotherapy. Their geometric integrity directly affects the accuracy of radiation delivery and the overall quality of treatment [14,15]. In the example of MLC tracking, MRIs are used to continuously modulate the radiation beam to maintain beam-to-target alignment. The use of distorted images to guide MLC tracking would cause the beam to be aligned with the distorted position of the target rather than the actual position. Secondly, patient positioning on MRI-Linacs is more restricted than on conventional linacs due to the size of the MRI bore. MRI-Linac patient couches have limited degrees of freedom and limited ranges of motion [16]. It is not always possible to locate the radiotherapy target at the isocentre and targets will often be located off-axis. As a result, radiation will more likely be delivered to areas affected by geometric distortion.

In this study, we implement a real-time distortion correction method on an MRI-Linac with MLC tracking to show that the effect of distortion can be removed to achieve accurate tracking of a radiotherapy target.

2. Materials and methods

This study utilised an end-to-end implementation of real-time distortion correction during adaptive radiotherapy with three main steps (Fig. 1): (1) the characterisation of the GNL distortion on the MRI-Linac, (2) integration of a fast distortion correction method with MLC tracking and (3) experimental validation during real-time adaptive radiotherapy using a motion phantom. The performance of our implementation was assessed by measuring the geometric accuracy of MLC tracking with and without distortion correction and the effect of the distortion correction method on tracking latency.

2.1. Experimental set-up

The method was implemented on the Australian MRI-Linac, a prototype MRI-Linac (Agilent, UK) that combines a 6 MV beam with a bespoke 1.0 T open-bore magnet and has been detailed in Liney *et al.* [17]. The open-bore magnet features a 50 cm gap that allows a patient to be set up perpendicular to the main magnetic field in addition to the conventional parallel geometry along the bore. While the open-bore magnet allows for greater flexibility in patient positioning, the gap in
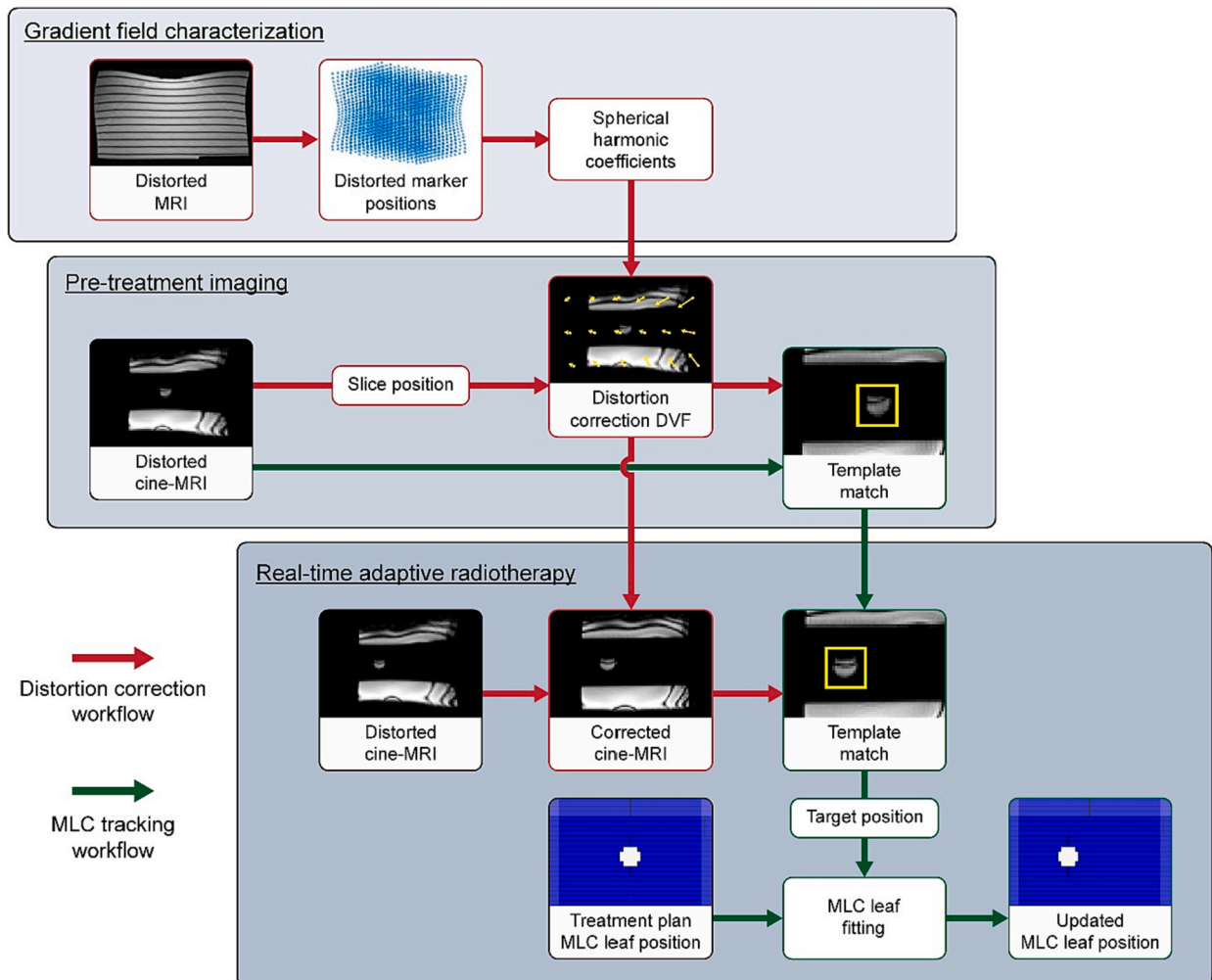

Fig. 1. The overall workflow for the implementation of real-time distortion correction (red arrows) with an existing MLC tracking workflow (green arrows).

the magnet introduces some imaging limitations. The diameter of spherical volume (DSV) which characterises the imaging volume is smaller and less homogenous (300 mm, ±4.05 ppm) than commercial MRI scanners (500 mm, ±1 ppm) and the split gradient coils make it more challenging to generate linear gradient fields (up to 5 % GNL within the DSV) [18].

For beam adaptation, the Australian MRI-Linac has a 120-leaf Millennium MLC (Varian, Palo Alto, CA, USA) which is modulated in real-time to perform MLC tracking of radiation targets [19]. As shown in Fig. 1, the MLC tracking algorithm takes the MLC leaf positions from an existing radiotherapy plan and for each new MRI acquisition, recalculates new MLC leaf positions based on the updated target position to maintain radiation beam-to-target alignment.

To test MLC tracking with real-time distortion correction, a Quasar motion phantom (Modus Medical Devices, Ontario, Canada) was set up at 3 positions on the Australian MRI-Linac: at isocentre (P_0), 165 mm (P_1) and 195 mm (P_2) from isocentre as shown in Fig. 2. These positions respectively represent a baseline with no distortion, a position at the edge of the DSV with visible distortions and a position outside the DSV with large distortions. Though the Australian MRI-Linac has not been certified to irradiate targets further than 150 mm from isocentre (i.e. outside the DSV), these locations were selected specifically to test the distortion correction method as the geometric distortion is clearly visible. From these initial positions, the target was moved in sinusoidally along the superior-inferior (SI) axis with period 10 s and amplitude 20 mm.

2.2. Gradient field characterisation

As a bespoke system, the Australian MRI-Linac does not have vendor-supplied distortion correction. The distortion of the MRI-Linac was characterised using spherical harmonics with the method previously described in Shan *et al.* [20]. A 20 cm × 20 cm × 30 cm grid phantom with 3,718 markers was imaged using turbo spin echo sequences on the MRI-Linac. These distorted images were segmented to give distorted marker positions which were compared to the undistorted ground truth positions from the construction specifications of the phantom. The marker positions were fit to 8th-order spherical harmonics to characterise the distortion field in the regions of interest [21].

2.3. Integration of distortion correction into MLC tracking workflow

To enable distortion correction during real-time adaptive radiotherapy, a fast image-domain based method of pixel re-mapping was integrated with the MLC tracking workflow, shown in Fig. 1. Prior to irradiation, a cineMRI image of the target, in this case a 30 mm sphere attached to the Quasar motion phantom was acquired in the tracking plane. DICOM metadata from this image (slice position, slice orientation and image resolution) was used to calculate a 2D distortion correction vector field based on the spherical harmonic coefficients.

The distortion vector field describes the in-plane distortion of each pixel in the pre-treatment cineMRI. Subsequent cineMRI frames acquired during real-time adaptive radiotherapy were rapidly corrected by applying the reverse of the vector field to re-map each pixel from its distorted position to its undistorted position. Bicubic interpolation was used for sub-pixel positions. The distortion correction vector field assumed the imaging plane remains static during irradiation and any change to the imaging plane required the distortion correction vector field to be recalculated.

2.4. Experimental verification of MLC tracking with distortion correction

MLC tracking of the target was performed with and without real-time distortion correction following the workflow in Fig. 1. Sagittal cineMRIs were acquired using the TRUFI sequence at 64 × 64 pixels (TR = 4.64 ms, TE = 2.31 ms, 610 Hz bandwidth, 300 mm field of view, 4.68 mm pixel size, 7 mm slice thickness) and 128 × 128 pixels (TR = 3.86 ms, TE = 1.92 ms, 610 Hz bandwidth, 300 mm field of view, 2.34 mm pixel size, 7 mm slice thickness). On each cineMRI, the target position relative to its starting position was calculated using template matching with the template delineated from the distortion corrected pre-treatment image. The change in position was then sent to a leaf-fitting algorithm that calculated updated MLC positions. Radiation was delivered from a fixed position along the LR axis in Fig. 2.

The geometric accuracy and latency of MLC tracking was evaluated from images of the treatment beam acquired with an electronic portal imaging device (EPID) using the method recommended by AAPM Task Group 264 [22] and detailed in Liu *et al.* [19]. The EPID simultaneously captured both the target centroid position and MLC aperture centroid
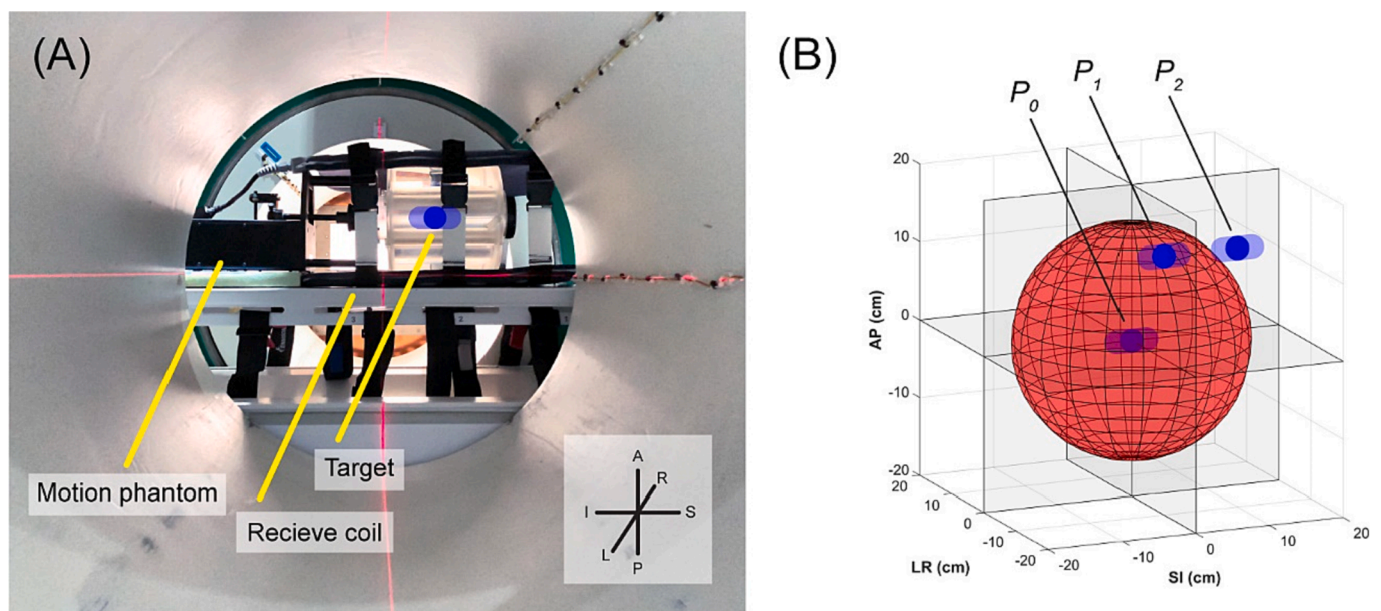

Fig. 2. (A) The motion phantom was set up in the gap of the open bore magnet, with the radiation beam parallel to the magnetic field and bore (along LR). The target motion is along the SI axis. (B) The positions of the motion phantom where MLC tracking was performed relative to the DSV of the MRI-Linac. The dark blue spheres indicate initial positions and light blue areas represent the ranges of motion.

positions, which were automatically segmented using in-house software. To remove latency as a source of error, sinusoids were fitted to both centroid curves and the phase difference between the two was calculated and subtracted. The latency-corrected root-mean-square error (RMSE) caused by geometric distortion was defined as the difference between the target centroid and the latency-adjusted MLC aperture centroid.

3. Results

3.1. Comparison of distortion corrected images

Fig. 3 shows corrected and uncorrected cineMRIs acquired during MLC tracking at each position. As parts of the phantom were outside of the DSV of the scanner, these images suffer from signal loss and banding artefacts due to the reduced B0 homogeneity of the magnetic field. Despite this, the geometric integrity of the target remained intact after distortion correction. The average normalised cross-correlation between the target template (acquired pre-treatment) and each corrected cineMRI was 0.98 at P_0, 0.94 at P_1 and 0.89 at P_2, indicating a high level of accuracy in the template matching step.

3.2. Geometric accuracy of distortion-corrected MLC tracking

Fig. 4 shows traces of the target centroid and the MLC aperture centroid during MLC tracking. At positions P_1 and P_2, geometric distortion caused the cineMRIs to expand and tracking the target without distortion correction resulted in the MLC leaves over-compensating for target motion at the peaks and troughs (most evident at P_2). With distortion correction applied, the MLC aperture centroids accurate follow the target centroids as they do at P_0 where distortion is negligible. The results have been corrected for latency to remove this error contribution, leaving the residual as the geometric accuracy.

The real-time distortion correction method reduced the geometric error at P_1 and P_2 to a level similar to tracking a target at isocentre (P_0). With 64×64 pixel images, the latency-corrected root-mean square error (RMSE) was reduced from 1.2 mm to 0.8 mm at P_1 and from 2.8 mm to 0.9 mm at P_2. This compares to a RMSE at P_0 of 1.0 mm. With 128×128 pixel images, the RMSE was reduced from 1.3 mm to 1.2 mm at P_1 and from 3.3 mm to 1.2 mm at P_2. This compares to a RMSE at P_0 of 0.9 mm. These results are shown in Fig. 5.

The maximum error was similarly reduced. With 64×64 pixel images, the maximum error was reduced from 2.6 mm to 1.84 mm at P_1 and from 6.0 mm to 2.6 mm at P_2. This compares to a maximum error at P_0 of 2.1 mm. With 128×128 pixel images, the maximum error was reduced from 3.4 mm to 2.9 mm at P_1 and from 6.4 mm to 2.7 mm at P_2. This compares to a maximum error at P_0 of 2.7 mm.

3.3. Computation times and latency

The pre-treatment calculation of the distortion correction vector field took ~ 250 ms for a 64×64 pixel images and ~ 850 ms for a 128×128 pixel images. Once the distortion correction vector field was calculated pre-treatment, subsequent correction of distortion for each cineMRI during real-time adaptive radiotherapy took < 10 ms. The end-to-end latency was measured to be 319 ± 12 ms for 64×64 pixel images and 540 ± 18 ms for 128×128 pixel images without distortion correction applied. With distortion correction applied, the latency was measured to be 335 ± 34 ms and 545 ± 18 ms respectively. Overall, the impact of distortion correction on latency was found to be within the uncertainty of measurement.

4. Discussion

In this work, we have developed a method of integrating fast distortion correction into a MRI-guided MLC tracking workflow. While the real-time distortion correction method requires an additional pre-treatment step, these computations have been automated and integrated into the workflow. We have shown that in cases where MR images of the radiotherapy target are affected by geometric distortion, this method successfully maintains tracking accuracy to the same level as tracking a target unaffected by distortion. The increase in tracking latency from the additional distortion correction step was less than the uncertainty of latency measurement and similar to previous work on the Australian MRI-Linac [19] and other systems in the literature [6,25].

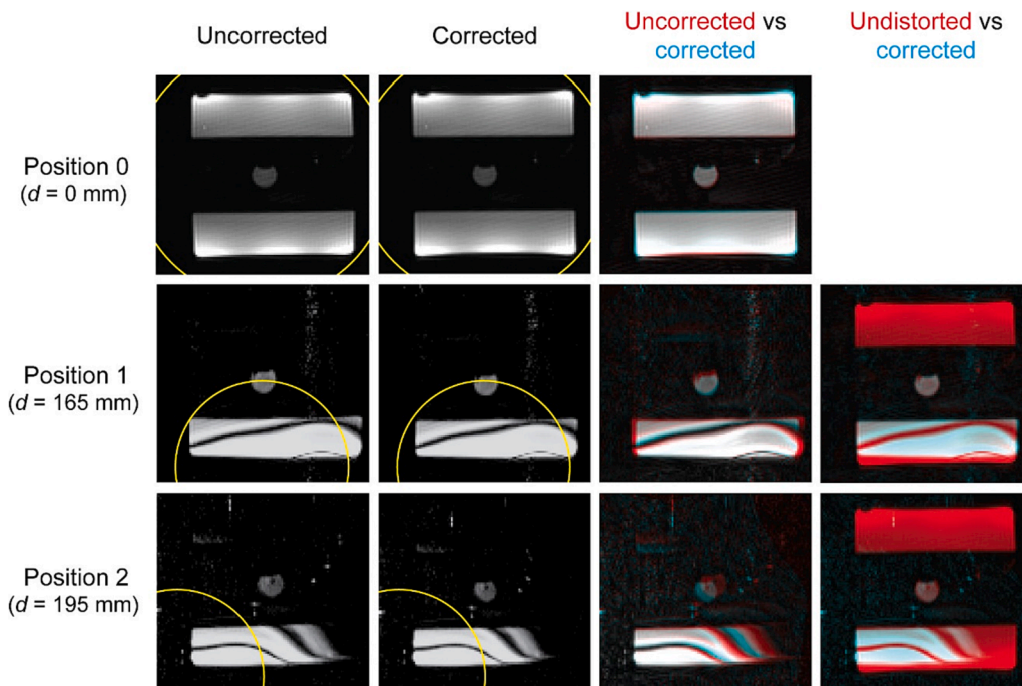A clinical implementation of the distortion correction method

Fig. 3. Corrected and uncorrected cineMRIs at each position (distance d from the isocenter) relative to the edge of the 300 mm DSV shown in yellow. Banding artifacts and loss of signal at P_1 and P_2 are expected for TRUFI acquisitions at the edge of the DSV due to reduced B0 homogeneity. The uncorrected vs corrected images have the uncorrected image in red and the corrected image in blue. The undistorted vs corrected images have the uncorrected image acquired at P_0 in red and the corrected image in blue.
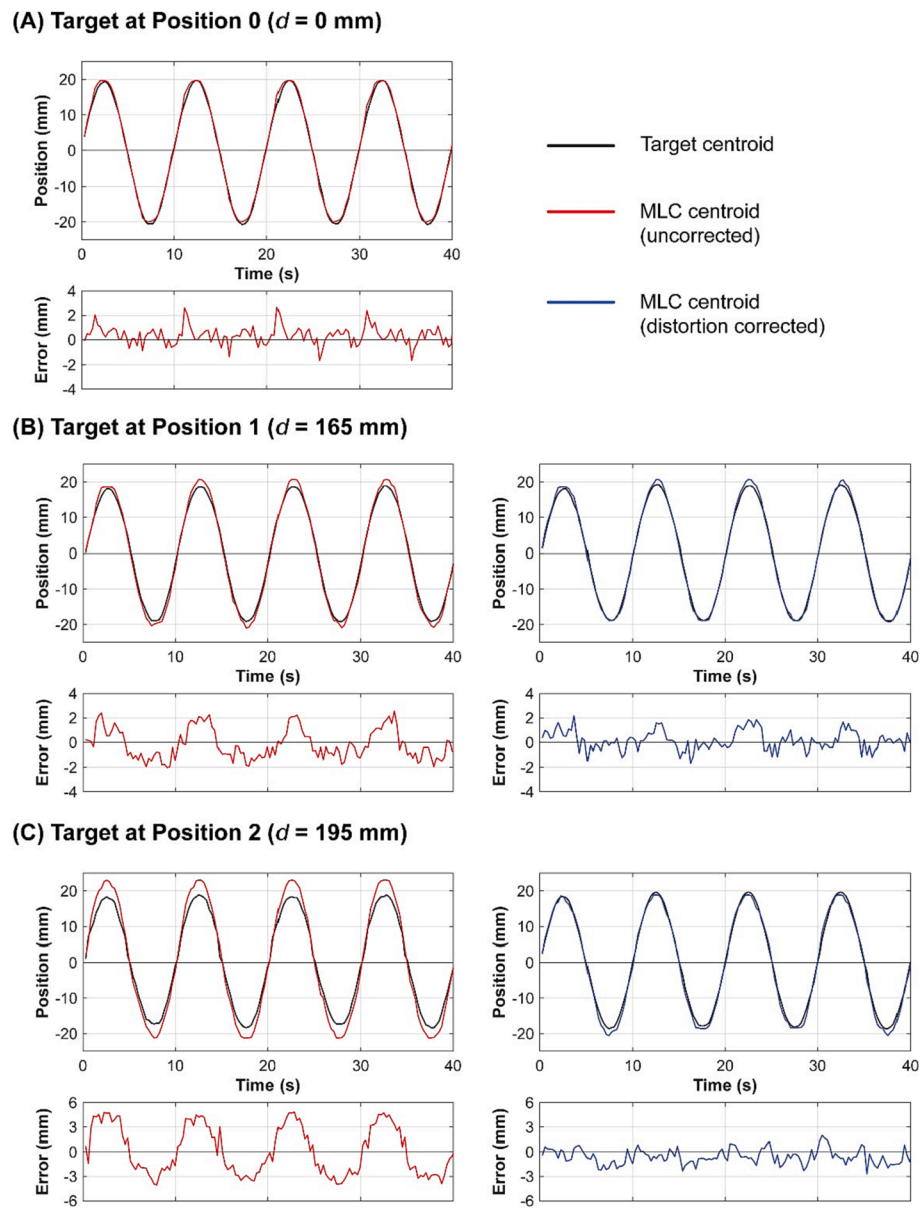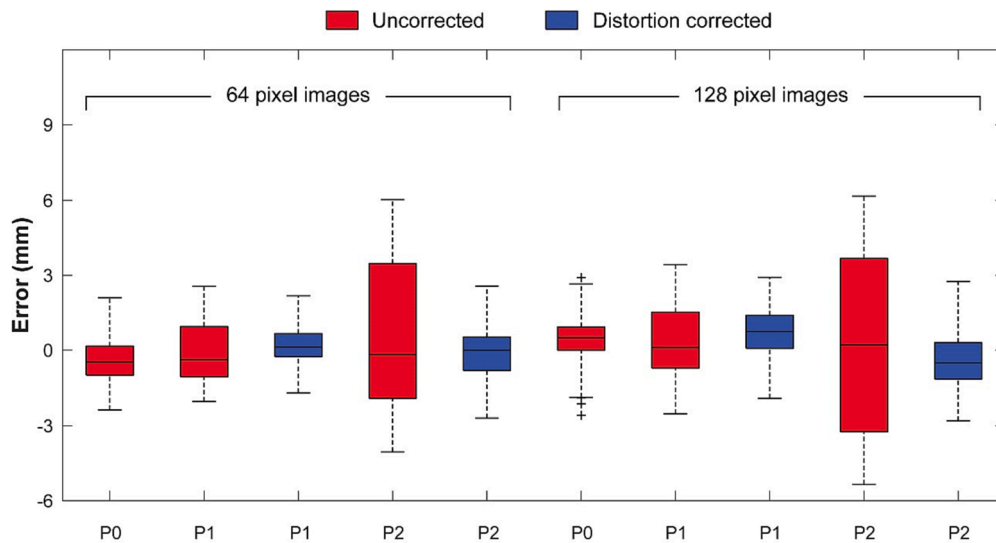
Fig. 4. Traces of target and MLC aperture centroids during MLC tracking with (in blue) and without (in red) real-time distortion correction. Traces are shown for tracking with 64 × 64 pixel images and MLC apertures have been corrected for latency to remove it as a source of error.

presented here could improve real-time MR-guided adaptive radiotherapy. Commercial MRI-Linac systems have not yet adopted MLC tracking capabilities and currently manage intrafraction motion through beam gating. Like MLC tracking, MR-guided beam gating can be negatively affected by geometric distortion [26]. Both the initial position of the target and the position of the target that triggers beam gating events can both suffer from inaccuracies due to geometric distortion. Applying a fast and accurate distortion correction for cineMRI would allow for smaller margins for off-axis targets that are treated with real-time adaptive radiotherapy. With the limitations on patient positioning within an MRI-Linac bore, it would also allow off-axis targets that previously could not be treated due to their distance from isocenter to be safely treated with real-time adaptation.

To achieve low latencies, the distortion correction method relied on the speed of image domain corrections. For large distortions, *k*-space domain corrections have been shown to produce distortion corrected images with higher image quality [8]. This is because pixel re-mapping in the image domain method cannot fully take into account pixels that become warped, enlarged, compressed or change shape. For patient anatomy with more complex structures and more varied contrast, *k*-space domain distortion corrections could produce more accurate target tracking. At present, the computation time for iterative *k*-space domain corrections can be several orders of magnitude greater than image domain corrections which limits its use in a real-time beam adaptation workflow. However, machine learning-based image reconstruction techniques that combine *k*-space domain distortion correction and image reconstruction into a single step can provide the highest image quality correction without any additional computation time [27].

One limitation of this work is that the distortion correction applied is a 2D correction that only corrects in-plane distortion. The geometry of these proof-of-concept experiments has the imaging plane orthogonal to the radiation beam and the target motion restricted to the imaging plane. However, there are situations where the radiation beam is at an angle that is not orthogonal to the imaging plane and 3D corrections are required to account for through-plane distortions. This could be solved by extending the method presented in this work from 2D to 3D by using a 3D distortion correction vector field and 3D voxel-remapping. However, if the through-plane distortion causes the target to distort out of the

Fig. 5. The distribution of residual errors between target and MLC aperture centroid positions compared to tracking at isocenter where distortion is minimal. Box plots represent the median, 25% and 75% points with the whiskers representing three standard deviations from the mean.

imaging plane, the correlation of target template matching could be degraded or the target could be entirely unseen. In this case, true 3D imaging with 3D distortion correction would be needed.

Though 3D distortion correction methods exist in the literature and have been used for radiotherapy, these methods generally are applied to pre-treatment images acquired as either 3D or 4D volumes that cover a single breathing cycle [28–30]. To achieve real-time 3D distortion correction during intrafraction imaging, true 3D cineMRI techniques are needed. Techniques such as simultaneous multi-slice imaging will become increasingly available on MRI-Linacs with the rapid progress in accelerated imaging techniques [31] and accelerated image reconstruction [32,33] and will enable a true 3D distortion correction that can account for a target distorting onto a different imaging plane.

These accelerated imaging techniques will also improve the overall accuracy of MLC tracking. For fast moving targets such as those in the abdomen, the tracking errors caused by geometric distortion are small compared to the tracking errors caused by system latency [19,25]. Therefore, while the image domain distortion correction method does not measurably increase the computation time, minimizing system latency though accelerated imaging or integrating motion prediction algorithms to mitigate tracking latency [34,35] should still be prioritised. After latency, the next largest source of error is the resolution limits of the cineMRIs. This can be seen at the peak positions of Fig. 4B, where the tracking errors occur as a result of the target appearing in between two pixels. Other sources of error include the imperfect GNL distortion correction at the edge of DSV, distortion caused by B0 inhomogeneity [23], template matching uncertainty, EPID segmentation uncertainty and the precision of the physical motion of the MLC leaves [24].

In summary, we have demonstrated a method to correct for geometric distortion during real-time adaptive radiotherapy accurately and without affecting end-to-end latency. We have shown that even in the presence of large distortions, the accuracy of MLC tracking was not degraded. A clinical implementation of this method would increase safety and confidence in performing real-time MR-guided radiotherapy particularly for targets that cannot be positioned at isocenter.

Declaration of Competing Interest

The authors declare that they have no known competing financial interests or personal relationships that could have appeared to influence the work reported in this paper.

Acknowledgements

References

[1] Keall PJ, Brighi C, Glide-Hurst C, Liney G, Liu PZY, Lydiard S, et al. Integrated MRI-guided radiotherapy – opportunities and challenges. Nat Rev Clin Oncol 2022;19: 458–70. https://doi.org/10.1038/s41571-022-00631-3.

[2] van Sornsen de Koste JR, Palacios MA, Bruynzeel AME, Slotman BJ, Senan S, and Lagerwaard FJ MR-guided Gated Stereotactic Radiation Therapy Delivery for Lung, Adrenal, and Pancreatic Tumors: A Geometric Analysis. Int J Radiat Oncol Biol Phys 2018;102:858-866. 10.1016/j.ijrobp.2018.05.048.

[3] Crijns SP, Raaymakers BW, Lagendijk JJ. Proof of concept of MRI-guided tracked radiation delivery: tracking one-dimensional motion. Phys Med Biol 2012;57: 7863–72. https://doi.org/10.1088/0031-9155/57/23/7863.

[4] Yun J, Wachowicz K, Mackenzie M, Rathee S, Robinson D, Fallone BG. First demonstration of intrafractional tumor-tracked irradiation using 2D phantom MR images on a prototype linac-MR. Med Phys 2013;40:051718. https://doi.org/10.1118/1.4802735.

[5] Hewson EA, Nguyen DT, O'Brien R, Poulsen PR, Booth JT, Greer P, et al. Is multileaf collimator tracking or gating a better intrafraction motion adaptation strategy? An analysis of the TROG 15.01 stereotactic prostate ablative radiotherapy with KIM (SPARK) trial. Radiother Oncol 2020;151:234–41. https://doi.org/10.1016/j.radonc.2020.08.010.

[6] Uijtewaal P, Borman PTS, Woodhead PL, Kontaxis C, Hackett SL, Verhoeff J, et al. First experimental demonstration of VMAT combined with MLC tracking for single and multi fraction lung SBRT on an MR-linac. Radiother Oncol 2022;174:149–57. https://doi.org/10.1016/j.radonc.2022.07.004.

[7] Weygand J, Fuller CD, Ibbott GS, Mohamed AS, Ding Y, Yang J, et al. Spatial Precision in Magnetic Resonance Imaging-Guided Radiation Therapy: The Role of Geometric Distortion. Int J Radiat Oncol Biol Phys 2016;95:1304–16. https://doi.org/10.1016/j.ijrobp.2016.02.059.

[8] Tao S, Trzasko JD, Shu Y, Huston 3rd J, Bernstein MA. Integrated image reconstruction and gradient nonlinearity correction. Magn Reson Med 2015;74: 1019–31. https://doi.org/10.1002/mrm.25487.

[9] Janke A, Zhao H, Cowin GJ, Galloway GJ, Doddrell DM. Use of spherical harmonic deconvolution methods to compensate for nonlinear gradient effects on MRI images. Magn Reson Med 2004;52:115–22. https://doi.org/10.1002/mrm.20122.

[10] Price RG, Kadbi M, Kim J, Balter J, Chetty IJ, Technical G-H, et al. Characterization and correction of gradient nonlinearity induced distortion on a 1.0 T open bore MR-SIM. Med Phys 2015;42:5955–60. https://doi.org/10.1118/1.4930245.

[11] Snyder JE, St-Aubin J, Yaddanapudi S, Boczkowski A, Dunkerley DAP, Graves SA, et al. Commissioning of a 1.5T Elekta Unity MR-linac: A single institution experience. J Appl Clin Med Phys 2020;21:160–72. https://doi.org/10.1002/acm2.12902.

[12] Hasler SW, Bernchou U, Bertelsen A, van Veldhuizen E, Schytte T, Hansen VN, et al. Tumor-site specific geometric distortions in high field integrated magnetic resonance linear accelerator radiotherapy. Phys Imaging Radiat Oncol 2020;15: 100–4. https://doi.org/10.1016/j.phro.2020.07.007.

[13] Alzahrani M, Broadbent DA, Chuter R, Al-Qaisieh B, Jackson S, Michael H, et al. Audit feasibility for geometric distortion in magnetic resonance imaging for radiotherapy. Phys Imaging Radiat Oncol 2020;15:80–4. https://doi.org/10.1016/j.phro.2020.07.004.

[14] Glide-Hurst CK, Paulson ES, McGee K, Tyagi N, Hu Y, Balter J, et al. Task group 284 report: magnetic resonance imaging simulation in radiotherapy: considerations for clinical implementation, optimization, and quality assurance. Med Phys 2021;48:e636-e670. 10.1002/mp.14695.

[15] Mengling V, Putz F, Laun FB, Perrin R, Eisenhut F, Dorfler A, et al. Evaluation of the influence of susceptibility-induced magnetic field distortions on the precision of contouring intracranial organs at risk for stereotactic radiosurgery. Phys Imaging Radiat Oncol 2020;15:91–7. https://doi.org/10.1016/j.phro.2020.08.001.

[16] Pappas E, Kalaitzakis G, Boursianis T, Zoros E, Zourari K, Pappas EP, et al. Dosimetric performance of the Elekta Unity MR-linac system: 2D and 3D dosimetry in anthropomorphic inhomogeneous geometry. Phys Med Biol 2019;64:225009. https://doi.org/10.1088/1361-6560/ab52ce.

[17] Liney GP, Dong B, Weber E, Rai R, Destruel A, Garcia-Alvarez R, et al. Imaging performance of a dedicated radiation transparent RF coil on a 1.0 Tesla inline MRI-linac. Phys Med Biol 2018;63:135005. https://doi.org/10.1088/1361-6560/aac813.

[18] Liu L, Sanchez-Lopez H, Poole M, Liu F, Crozier S. Simulation and analysis of the interactions between split gradient coils and a split magnet cryostat in an MRI-PET system. J Magn Reson 2012;222:8–15. https://doi.org/10.1016/j.jmr.2012.05.022.

[19] Liu PZY, Dong B, Nguyen DT, Ge Y, Hewson EA, Waddington DEJ, et al. First experimental investigation of simultaneously tracking two independently moving targets on an MRI-linac using real-time MRI and MLC tracking. Med Phys 2020;47: 6440–9. https://doi.org/10.1002/mp.14536.

[20] Shan S, Liney GP, Tang F, Li M, Wang Y, Ma H, et al. Geometric distortion characterization and correction for the 1.0 T Australian MRI-linac system using an inverse electromagnetic method. Med Phys 2020;47:1126–38. https://doi.org/10.1002/mp.13979.

[21] Weavers PT, Tao S, Trzasko JD, Shu Y, Tryggestad EJ, Gunter JL, et al. Image-based gradient non-linearity characterization to determine higher-order spherical harmonic coefficients for improved spatial position accuracy in magnetic resonance imaging. Magn Reson Imaging 2017;38:54–62. https://doi.org/10.1016/j.mri.2016.12.020.

[22] Keall PJ, Sawant A, Berbeco RI, Booth JT, Cho B, Cervino LI, et al. AAPM Task Group 264: The safe clinical implementation of MLC tracking in radiotherapy. Med Phys 2020. https://doi.org/10.1002/mp.14625.

[23] Keesman R, van der Bijl E, Janssen TM, Vijlbrief T, Pos FJ, and van der Heide UA Clinical workflow for treating patients with a metallic hip prosthesis using magnetic resonance imaging-guided radiotherapy. Phys Imaging Radiat Oncol 2020;15:85-90. 10.1016/j.phro.2020.07.010.

[24] Caillet V, Zwan B, Briggs A, Hardcastle N, Szymura K, Prodreka A, et al. Geometric uncertainty analysis of MLC tracking for lung SABR. Phys Med Biol 2020;65: 235040. https://doi.org/10.1088/1361-6560/abb0c6.

[25] Glitzner M, Woodhead PL, Borman PTS, Lagendijk JJW, Raaymakers BW. Technical note: MLC-tracking performance on the Elekta unity MRI-linac. Phys Med Biol 2019;64:15NT02. https://doi.org/10.1088/1361-6560/ab2667.

[26] Ginn JS, Agazaryan N, Cao M, Baharom U, Low DA, Yang Y, et al. Characterization of spatial distortion in a 0.35 T MRI-guided radiotherapy system. Phys Med Biol 2017;62:4525–40. https://doi.org/10.1088/1361-6560/aa6e1a.

[27] Shan S, Gao Y, Liu PZ, Whelan B, Sun H, Dong B, et al. Distortion-Corrected Image Reconstruction with Deep Learning on an MRI-Linac. arXiv preprint arXiv: 2205.10993 2022.

[28] Tanner SF, Finnigan DJ, Khoo VS, Mayles P, Dearnaley DP, Leach MO. Radiotherapy planning of the pelvis using distortion corrected MR images: the removal of system distortions. Phys Med Biol 2000;45:2117–32. https://doi.org/10.1088/0031-9155/45/8/305.

[29] Baldwin LN, Wachowicz K, Thomas SD, Rivest R, Fallone BG. Characterization, prediction, and correction of geometric distortion in 3 T MR images. Med Phys 2007;34:388–99. https://doi.org/10.1118/1.2402331.

[30] Keesman R, van de Lindt TN, Juan-Cruz C, van den Wollenberg W, van der Bijl E, Nowee ME, et al. Correcting geometric image distortions in slice-based 4D-MRI on the MR-linac. Med Phys 2019;46:3044–54. https://doi.org/10.1002/mp.13602.

[31] Keijnemans K, Borman PTS, Uijtewaal P, Woodhead PL, Raaymakers BW, Fast MFA. hybrid 2D/4D-MRI methodology using simultaneous multislice imaging for radiotherapy guidance. Med Phys 2022;49:6068–81. https://doi.org/10.1002/mp.15802.

[32] Kustner T, Fuin N, Hammernik K, Bustin A, Qi H, Hajhosseiny R, et al. CINENet: deep learning-based 3D cardiac CINE MRI reconstruction with multi-coil complex-valued 4D spatio-temporal convolutions. Sci Rep 2020;10:13710. https://doi.org/10.1038/s41598-020-70551-8.

[33] Waddington DE, Hindley N, Koonjoo N, Chiu C, Reynolds T, Liu PZ, et al. On Real-time Image Reconstruction with Neural Networks for MRI-guided Radiotherapy. arXiv preprint arXiv:2202.05267 2022.

[34] Johl A, Ehrbar S, Guckenberger M, Klock S, Meboldt M, Zeilinger M, et al. Performance comparison of prediction filters for respiratory motion tracking in radiotherapy. Med Phys 2020;47:643–50. https://doi.org/10.1002/mp.13929.

[35] Lombardo E, Rabe M, Xiong Y, Nierer L, Cusumano D, Placidi L, et al. Offline and online LSTM networks for respiratory motion prediction in MR-guided radiotherapy. Phys Med Biol 2022:67. https://doi.org/10.1088/1361-6560/ac60b7.